Molecular Catalysis 585 (2025) 115332

Contents lists available at ScienceDirect

Molecular Catalysis

journal homepage: www.journals.elsevier.com/molecular-catalysis

Research Paper

Enhancing CO_2 methanation over Rh catalyst supported on ZrO_2 cubic phase stabilized by MgO addition

F. Ayala-Flores [a], R. Huirache-Acuña [a], A. Solís-Garcia [b], J.C. Fierro-Gonzalez [c], Daviel Gómez [d], Patricia Concepción [d], G. Berhault [e], S. Gil [e], D.Y. López-Chico [f], E. García-Bordejé [g], T.A. Zepeda [b,*]

[a] División de Estudios de Posgrado de la Facultad de Ingeniería Química, Universidad Michoacana de San Nicolás de Hidalgo, Gral. Francisco J. Múgica S/N, Morelia, Mich., 58004, Mexico
[b] Centro de Nanociencias y Nanotecnología. Universidad Nacional Autónoma de México. Ensenada, B. C. 22800, Mexico
[c] Departamento de Ingeniería Química, Tecnológico Nacional de México en Celaya, Av. Tecnológico y Antonio García Cubas s/n. Celaya, Guanajuato 38010, Mexico
[d] Instituto de Tecnología Química, Universitat Politècnica de València - Consejo Superior de Investigaciones Científicas (UPV-CSIC), Avenida de los Naranjos s/n, 46022, Valencia, Spain
[e] Institut de Recherches sur la Catalyse et l'Environnement, CNRS – Université Lyon I, Villeurbanne, 69626, France
[f] Centro de Investigación de Ciencia y Tecnología Aplicada de Tabasco, Universidad Juárez Autónoma de Tabasco, Carretera Cunduacán–Jalpa de Méndez Km. 1, Cunduacán, 86690, Mexico
[g] Instituto de Carboquímica (ICB-CSIC), Miguel Luesma Castán 4, E-50018 Zaragoza, Spain

ARTICLE INFO

Keywords:
CO_2 Methanation
Reaction mechanism
Supported rhodium catalysts
Magnesium oxide
Operando FTIR

ABSTRACT

Here, it reports the influence of MgO incorporation on the structural and catalytic properties of Rh catalysts supported on ZrO_2 for CO_2 methanation. The results show that MgO addition promotes the formation of the cubic phase of ZrO_2, leading to an increase in surface area, oxygen vacancies, and surface basicity, factors that collectively enhance CO_2 adsorption and activation under reaction conditions. Catalytic testing revealed that a low MgO content (1.7 wt %) yielded the highest CO_2 conversion (37.8 % at 325 °C), while higher MgO loadings resulted in decreased activity. Notably, the catalyst with the highest MgO content (5.5 wt %) exhibited remarkably low CO selectivity (1.4 %), indicating suppression of the reverse water-gas shift (RWGS) reaction in favor of the associative methanation pathway. This behavior is related to the increase in surface basicity, which significantly influences the nature of surface intermediates during the reaction, favoring methane formation via direct CO_2 hydrogenation. In situ FTIR analysis confirmed the presence of key intermediates, such as formate and Rh°–carbonyl species. As MgO content increased, the formation of Rh^0–carbonyl species diminished, further promoting selectivity toward methane.

1. Introduction

Climate change and global warming are among the most pressing challenges facing humanity today, primarily driven by the increasing atmospheric concentration of greenhouse gases, particularly carbon dioxide. This rise is largely attributed to fossil fuel combustion, which continues to meet society energy demands [1,2]. In response, research about CO_2 utilization technologies has intensified, the CO_2 methanation (Sabatier reaction) emerging as a promising strategy for reducing the atmospheric CO_2 concentrations [3,4]. This process not only helps mitigate greenhouse gas emissions but also produces methane, a valuable clean fuel and energy carrier [3].

However, the inherent thermodynamic stability of the CO_2 molecule, combined with the exothermic nature of CO_2 methanation ($\Delta H^{298K} = -164$ kJ/mol), leads to an increase in reaction temperature, which negatively impacts CO_2 conversion by affecting the reaction chemical kinetics [5]. This makes the process more challenging, with the primary difficulty being the design of catalysts that can efficiently catalyze CO_2 methanation at lower temperatures while achieving high conversion rates and suppressing side reactions such as the reverse water-gas shift and CO hydrogenation [5,6].

Typical catalysts for CO_2 methanation consist of precious and

* Corresponding authors.
E-mail address: trino@ens.cnyn.unam.mx (T.A. Zepeda).

https://doi.org/10.1016/j.mcat.2025.115332
Received 6 May 2025; Received in revised form 17 June 2025; Accepted 2 July 2025
Available online 8 July 2025

transition metals dispersed on various metal oxide supports. Metals such as Ru, Rh, Pd, and Ni [7–10], supported on oxides like Al_2O_3, CeO_2, SiO_2, TiO_2 and ZrO_2 [11–13], have been extensively studied by various research groups to optimize catalytic performance and stability. Among the catalysts mentioned, despite its high cost, supported Rh catalysts remains one of the most promising options for CO_2 methanation, due to its great catalytic activity and selectivity for methane formation at low temperatures [4].

Although CO_2 methanation may seem like a simple reaction, it follows two well-recognized mechanistic pathways, which can even coexist [14]. The first is the association pathway, where CO_2 molecules adsorb onto the catalytic support as carbonates and undergo subsequent reduction, leading to the formation of formate species, a key reaction intermediate [14,15]. The second pathway involves CO_2 dissociation via the reverse water-gas shift (RWGS) reaction, producing adsorbed carbonyl species, followed by a reduction, ultimately yielding methane and water [15,16]. Therefore, developing catalysts capable of achieving efficient low-temperature CO_2 methanation while effectively suppressing the RWGS reaction and minimizing CO formation remains a significant challenge, which would have a significant impact on hydrogen consumption during the reaction [4,5]

In this respect, ZrO_2 has gained a significant attention as a support material for Rh catalysts in CO_2 methanation, owing to its strong CO_2 adsorption capacity and moderate acid-base surface properties. These characteristics promote effective Rh dispersion and facilitate the conversion of CO_2-derived adsorbed species on ZrO_2 into formate intermediates, which play a pivotal role in the methanation process [17,18].

ZrO_2 is a polycrystalline material that can exist in three principal crystallographic phases: monoclinic (m), tetragonal (t), and cubic (c), each with distinct structural features that impact its catalytic behavior. Regularly the m-ZrO_2, t-ZrO_2 or their mixtures have been employed as supports for Rh-based catalysts in CO_2 methanation [14,19,20] reported that cubic ZrO_2 can promotes the CO_2 methanation via formate pathway avoiding the CO formation via RWGS reaction. Additionally, t-ZrO_2 can undergo a spontaneous transformation into the monoclinic phase when exposed to relatively low temperatures (65–400 °C) in the presence of water vapor leading a significant loss in the dispersion of the active phase, promoting the sintering of rhodium species [18]. As a result, the contribution of rhodium to the overall CO_2 methanation activity is diminished. On the other hand, c-ZrO_2 has been shown to maintain structural stability under reaction conditions and exhibit resistance to water vapor-induced transformation [21]. Therefore, stabilizing ZrO2 in its cubic phase presents a promising strategy for enhancing the durability and performance of Rh-based catalysts in CO_2 methanation.

Some studies have shown that the addition of MgO [22], Y_2O_3 [23], CaO [24], and CeO_2 [25] promotes the formation of partially stabilized zirconia (PSZ), where the cubic phase becomes predominant. This stabilization strategy offers a promising pathway to enhance catalyst stability and performance in CO_2 methanation applications.

The incorporation of MgO has been observed to have a beneficial effect on CO and CO_2 methanation reactions by increasing the number of basic sites, thereby enhancing CO_2 adsorption and activation as surface carbonate species [26,27]. Additionally, MgO promotes the formation of the cubic crystalline phase of ZrO_2, which is more stable and can improve the methanation of carbon oxides via formate route [28].

Based on these findings, this study investigates the effect of MgO incorporation on the formation of the cubic phase of ZrO_2 as a support for Rh catalysts in CO_2 methanation. Furthermore, the nature of surface species formed during the reaction was analyzed using FTIR spectroscopy under operating conditions to elucidate the role of magnesium in the reaction mechanism.

2. Experimental

2.1. Synthesis of supports and catalysts

ZrO_2 was synthesized using the precipitation method. The procedure involved the dropwise addition of a 1 M aqueous NH_4OH solution (Sigma-Aldrich) at room temperature to a 0.1 M solution of ZrO $(NO_3)_2{\cdot}xH_2O$ (Sigma-Aldrich). MgO-ZrO_2 can be obtained in a similar way using a 0.1 M mixture of $ZrO(NO_3)_2$ (Sigma-Aldrich, 99 %) with the desired amount of $Mg(NO_3)_2{\cdot}6H_2O$ (Sigma-Aldrich, 99 %). The addition was carried out under constant stirring until the pH of the mixture reached approximately 10. A white precipitate was formed, which was aged for 1 h and then filtered and washed with deionized water. Subsequently, the resulting powder was dried overnight at 100 °C and then it was calcined at 500 °C for 5 h. The MgO-ZrO_2 mixed oxides supports were synthesized with varying MgO contents of 1.7 %, 3.5 %, and 5.5 % by weight, corresponding to Mg:Zr molar ratios of 5:95, 10:90, and 15:85, respectively.

Rhodium catalysts supported on the oxides were prepared using the excess impregnation method. During synthesis, the support was exposed to an aqueous $RhCl_3$ solution for 1 h at room temperature. The solvent was then removed by stirring at 80 °C, followed by drying at 120 °C for 12 h and calcination in air at 450 °C for 5 h. The solution concentration was calculated to achieve a metal loading of 1 wt %.

2.2. Catalysts characterization

X-ray diffraction characterization was performed using a PANalytical Aeris diffractometer equipped with a Pixel 1D detector and a Cu Kα radiation source (λ = 1.5405 Å), with a step size of 0.02 °/s, from 10 to 80° (2θ).

Textural properties were evaluated using the N_2 adsorption-desorption isotherms at −196 °C on a Micromeritics TRISTAR III system. Before the analysis, samples were pre-treated by outgassing at 300 °C for 3 h. The Brunauer–Emmett–Teller method was used for surface area calculations, and the pore size distribution was calculated using DFT Plus software (Micromeritics) using the Barrett–Joyner–Halenda (BJH) model with cylindrical pore geometry.

CO_2- and O_2-TPD desorption experiments for the freshly reduced catalysts were carried out in a U-shaped quartz reactor coupled to a Hidden HAL301 on-line analytical mass spectrometer (MS). Before to the desorption test, 40 mg of the catalysts were reduced *in-situ* at 300 °C for 1 h in a stream of H_2 (40 mL/min), and finally the temperature was increased up to 400 °C in a stream of He (80 mL/min) for 1 h to remove H_2 likely to be adsorbed on the catalyst surface.

For the CO_2-TPD analysis, after purging the H_2 adsorbed during the reduction process, the catalyst was cooled to 100 °C under a He flow (80 $mLmin^{-1}$). The samples were then exposed to CO_2 (30 $mLmin^{-1}$) at this temperature for 60 min. Subsequently, they were purged again with He (80 $mLmin^{-1}$) for 40 min, cooled to 40 °C under He flow, and then heated from 40 °C to 750 °C under He flow at a rate of 5 $°Cmin^{-1}$, while monitoring CO_2 desorption.

For the O_2-TPD analysis, after purging the H_2 adsorbed during the reduction process, the catalyst was cooled to 40 °C under a He flow (80 $mLmin^{-1}$). Then the oxygen adsorption was carried out at this temperature for 2 h in an atmosphere containing 1 % O_2 in He. Subsequently, the sample was purging with He for 45 min, then the TPD was performed under a continuous He flow with a temperature ramp of 5 °C min^{-1}.

UV–Vis absorption spectra of the freshly reduced catalysts were obtained using a Cary Series UV–Vis-NIR spectrophotometer equipped with a sphere of integration. The samples were reduced in situ at 300 °C for 1 h in a stream of H_2 (40 mL/min).

Temperature-programmed reduction (TPR) analyses were conducted using a Quantachrome ChemBET Pulsar equipment. About 30 mg of the sample was first degassed at 150 °C under a N_2 flow for 1 h. After cooling to room temperature, the TPR analysis was performed by heating the

sample in a U-tube reactor to 600 °C at 10 °C/min in a 10 % H_2/Ar mixture at 25 mL/min.

TEM analyses were performed using a JEOL JEM 2010 electron microscope working at 200 kV with a point resolution of 2.35 Å. High-angle annular dark-field scanning transmission electron microscopy (HAADF-STEM) setup and energy dispersive X-ray spectroscopy (EDX) were used simultaneously to analyze the elemental composition of the catalysts, employing a Euro EA3000 elemental analyzer (EuroVector) with sulfanilamide as a reference.

2.3. FTIR characterization under reaction conditions

Surface species were characterized by infrared spectroscopy (FTIR) under reaction conditions using an Agilent Cary 660 spectrophotometer equipped with an ISRI cell/reactor. Self-supported catalyst wafers with a thickness of 35 mg/cm^2 were prepared by pressing the powder samples under a pressure of 7×10^3 kg/m^2. The self-supported wafer was treated with a reducing mixture of H_2 (10 mL/min) and N_2 (5 mL/min) at 300 °C for 1 h and then cooled to room temperature. The previously in situ reduced samples were subjected to a flow of H_2 (10 mL/min) and CO_2 (2.5 mL/min) while the cell/reactor temperature was increased by 2 °C/min from room temperature to 300 °C. Simultaneously, IR spectra were collected every 50 °C from 150 °C with a resolution of ± 4 cm^{-1} in the range from 4000 to 950 cm^{-1}.

2.4. Catalytic activity

The catalytic activity of the samples was evaluated in a quartz reactor with an internal diameter of 4 mm coupled to an on-line gas chromatograph (Clarus 690 GC) equipped with 2 columns (HAYESEP P and MOLE SIEVE 5A) and 2 detectors (TCD and FID). For the experiments, 60 mg of catalyst was diluted with the appropriate mass of silicon carbide to reach a total volume of 1 cm^3. Prior to catalytic tests, the samples were reduced in situ at 300 °C for 1 h in a stream of H_2 (40 mL/min). The gas flow was then switched to a reactive mixture of 20 % CO_2 and 80 % H_2 v/v, achieving a 1:4 molar ratio of CO_2:H_2. The gas hourly space velocity (GHSV) was set at 30,000 h^{-1} for these experiments. The catalytic activity was evaluated over a temperature range from 175 °C to 325 °C by recording different chromatograms every 25 °C. Catalytic activity was evaluated by CO_2 conversion and selectivity towards CH_4/CO products at stationary conditions from 175 °C to 325 °C.

The catalytic activity of the materials was calculated using the CO_2 inflow and outflow using the following equation:

$$X_{CO_2}(\%) = \frac{F^{in}_{CO_2} - F^{out}_{CO_2}}{F^{in}_{CO_2}} * 100 \quad (1)$$

The selectivity of the reaction towards methane was calculated by the following equation:

$$S_{CH_4}(\%) = \frac{F^{out}_{CH_4}}{F^{in}_{CO_2} - F^{out}_{CO_2}} * 100 \quad (2)$$

$$S_{CO}(\%) = \frac{F^{out}_{CO}}{F^{in}_{CO_2} - F^{out}_{CO_2}} * 100 \quad (3)$$

3. Results and discussion

The catalysts were labeled as CZr for the magnesium oxide-free catalyst, while those with Mg:Zr molar ratios of 5:95, 10:90, and 15:85 were labeled CZrMg5, CZrMg10, and CZrMg15, respectively.

3.1. Catalysts characterization

The chemical composition of the Rh catalysts supported on mixed oxides, as determined by ICP-OES, is presented in Table 1. The magnesium content, expressed as MgO, was 1.7, 3.5, and 5.5 wt. % for the CZrMg5, CZrMg10, and CZrMg15 catalysts, respectively. The Rh loading ranged from 0.95 to 0.97 wt. %, in close agreement with the nominal value of 1 wt. % specified in the experimental section.

Table 1
Chemical composition (obtained from ICP-OES) and textural properties of the rhodium catalysts supported on ZrO_2 and on zirconium-magnesium mixed oxides.

Sample	Mg:Zr molar ratio	MgO (wt. %)	Rh (wt. %)	S_{BET} (m^2/g)	V_p (cm^3/g)	D_p (nm)
CZr	-	-	0.97	60	0.12	6.8
CZrMg5	5	1.7	0.95	85	0.13	5.1
CZrMg10	10	3.5	0.97	85	0.10	4.1
CZrMg15	15	5.5	0.96	77	0.07	3.7

Textural properties were also determined following N_2 adsorption-desorption measurements. According to the IUPAC classification, all materials exhibited type IV N_2 adsorption-desorption isotherms (data not shown here), characteristic of mesoporous materials [4]. The textural properties of the materials, obtained from N_2 adsorption-desorption isotherms at −196 °C, are summarized in Table 1. The MgO-free catalyst exhibited the lowest surface area (S_{BET}) among the catalysts studied. The incorporation of MgO led to an increase in surface area, with CZrMg5 and CZrMg10 catalysts displaying similar S_{BET} values (85 m^2/g), compared to the MgO-free catalyst (60 m^2/g). However, at higher MgO concentrations, a slight decrease in S_{BET} was observed, with the CZrMg15 catalyst with a surface area of 77 m^2/g.

The pore volume (Vp) remained relatively unchanged between the MgO-free catalyst and the catalyst with the lowest MgO content (CZrMg5). However, as the MgO content increased, Vp showed a significant decline, reaching its lowest value in the CZrMg15 catalyst. Additionally, the average pore diameter (Dp) gradually decreased with increasing MgO content, from 6.8 nm in the CZr catalyst to 3.7 nm in the CZrMg15 catalyst, which had the highest MgO concentration. It is important to note that the porosity in these materials arises from both the pores formed within the particles and the intrinsic porosity of the crystal structure, both of which contribute to the total porosity. The reduction in pore size may be linked to an increase in crystal size, as evidenced by X-ray diffraction patterns, leading to a notable decrease in both overall porosity and average pore diameter.

The X-ray diffraction characterization of the Rh catalysts supported on mixed oxides are shown in Fig. 1. The diffraction patterns of the MgO-

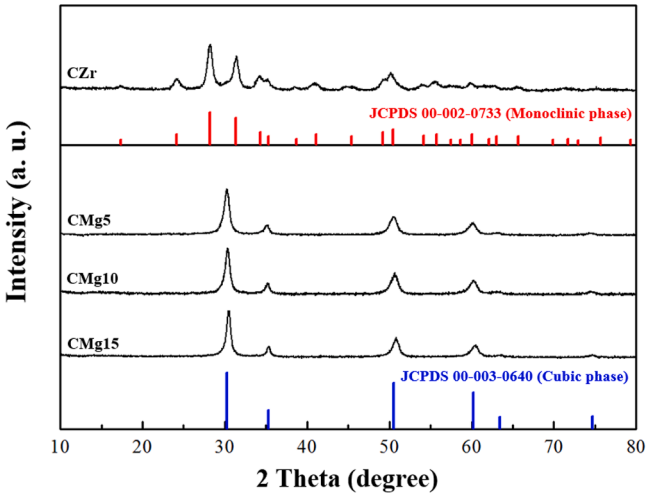

Fig. 1. X-ray diffraction patterns of the rhodium catalysts supported on ZrO_2 and zirconium-magnesium mixed oxides. The letters M, T and C denote the peaks corresponding to monoclinic zirconia and cubic zirconia-magnesium oxide respectively.

free RhZr catalyst exhibit characteristic peaks corresponding to monoclinic (JCPDS 00–001–0750) ZrO_2 phase. The incorporation of magnesium oxide induces significant crystallographic modifications in the ZrO_2 structure. Catalysts containing MgO exhibit well-defined diffraction peaks characteristic of the cubic phase of ZrO_2 (Fig. 1). The addition of MgO promotes the formation of a highly stable cubic ZrO_2 structure (JCPDS 00–003–0640). Notably, no diffraction patterns corresponding to magnesium oxide or rhodium particles (metallic or oxide) were observed. This suggests that these species may be present in sizes below the detection limit of the X-ray diffraction technique or exist in an amorphous state (for MgO). Furthermore, the incorporation of MgO enhances the crystallinity of zirconium oxide, as observed in Fig. 1, where the diffraction peaks exhibit greater intensity and improved definition. The cubic phase of ZrO_2 is highly desirable, as it has been reported to enhance CO_2 methanation over rhodium catalysts while also exhibiting excellent stability in the presence of water vapor generated during the reaction [29,30].

The average crystal size of the ZrO_2 phases was determined using the Scherrer equation. For the MgO-free CZr catalyst, the calculated crystal size was 12.2 nm fo. The incorporation of MgO not only promotes the formation of the cubic phase of ZrO_2 but also contributes to the development of smaller crystals. The smallest crystal size was observed in the CZrMg10 sample, with an average size of 9.8 nm, followed by the CZrMg5 catalyst, which had an average size of 11 nm. In contrast, the CZrMg15 catalyst, which contained the highest MgO content, exhibited a slightly larger average crystal size of 13.3 nm.

The CO_2-TPD experiment for the freshly reduced catalysts was performed to verify the enhancement of basic site content due to the addition of MgO as a promoter. The CO_2-TPD profiles of the catalysts are presented in Fig. 2. CO_2-TPD desorption profiles are typically analyzed across three temperature ranges. The first desorption region, occurring at low temperatures (100–250 °C), is attributed to weakly basic Brønsted sites, such as surface OH groups. The second region, at medium temperatures (250–400 °C), corresponds to medium-strength Lewis base sites. Finally, the third desorption stage, observed at temperatures above 400 °C, is associated with low-coordination oxygen anions, which function as strong basic sites [31].

The MgO-free catalyst (CZr) exhibited two well defined CO_2 desorption peaks at 98 °C and 240 °C corresponding therefore respectively to weakly basic Brønsted sites and medium-strength Lewis basic sites. The first peak corresponds to weakly basic Brønsted sites, while the second, at 240 °C, is associated with medium-strength Lewis acid-base sites. Additionally, the CZr catalyst displayed the lowest CO_2-TPD signal intensity, indicating a reduced capacity for CO_2 adsorption on its surface.

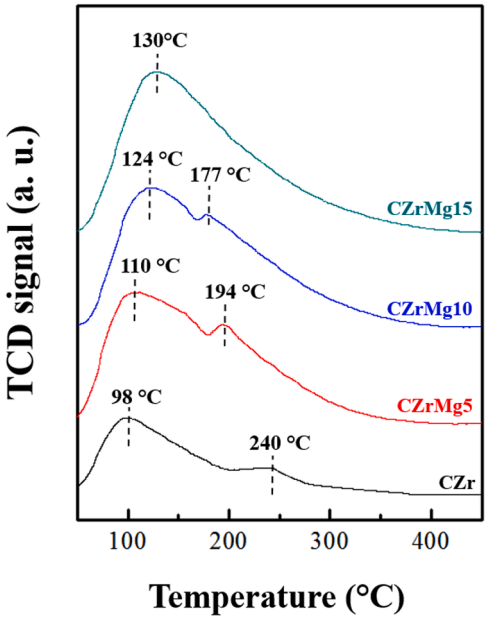

Fig. 2. CO_2 -TPD profile for the freshly reduced rhodium catalysts supported on ZrO_2 and zirconium-magnesium mixed oxides.

In contrast, the incorporation of MgO significantly increased the amount of desorbed CO_2, suggesting that the presence of this alkaline compound enhances CO_2 capture on the surface. This improvement may be attributed to an increase in surface basicity, resulting from the presence of MgO species and/or the formation of additional oxygen vacancies (vide infra, UV–Vis DRS analyses), both of which contribute to CO_2 adsorption. All MgO-containing catalysts exhibit a broad and intense CO_2 desorption peak centered between 110 and 130 °C. The MgO-free catalyst exhibited the lowest temperature for the main CO_2 desorption peak. As the MgO loading increased, the temperature of this principal desorption peak was shifted higher temperatures. The highest desorption temperature, 130 °C, was observed for the catalyst with the greatest MgO content (CZrMg15). This suggests that at higher MgO concentrations, the interaction between CO_2 molecules and the surface is stronger compared to catalysts with MgO-free sample. However, as the MgO content increases, the interaction strength slightly weakens. This effect could be attributed to the formation of basicity sites on the surface promoted by the MgO species.

Additionally, a signal at higher temperatures was observed on the CZr, CZrMg5 and CZrMg10catalysts, appearing at 240 °C, 194 °C and 177 °C, respectively. These signals are attributed to medium-intensity acid-base sites, originating from unsaturated Zr^{4+}-O^{2-} and Mg^{4+}-O^{2-} pairs [32]. The intensity of this signal decreased and shifted to lower temperatures with increasing MgO content. Notably, this signal was not observed for the catalyst with the highest MgO content, suggesting that increasing MgO concentration leads to the generation of a greater number of strong basic sites, while medium-strength basic sites become less TCD signal. This effect may be attributed to the partial coverage of the zirconia surface by MgO species.

The amount of desorbed CO_2 was approximately 2.2 times higher in the MgO-containing samples compared to the MgO-free sample. The alkali content was calculated based on the data from Fig. 2. The total basicity of the sites follows the order: CZrMg15 (112 μmol CO_2 g_{cat}^{-1}) > CZrMg10 (101 μmol CO_2 g_{cat}^{-1}) > CZrMg5 (95 μmol CO_2 g_{cat}^{-1}) >> CZr (62 μmol CO_2 g_{cat}^{-1}). These results indicate that the presence of MgO significantly enhances the CO_2 adsorption capacity compared to the catalyst without MgO. Additionally, although no substantial differences are observed in the total amount of CO_2 adsorbed among the catalysts containing MgO, there are notable variations in the nature of basic sites present on the surface.

The O_2-TPD experiment was conducted on freshly reduced catalysts after oxygen saturation, as described in the experimental section, to confirm the enhancement in oxygen storage capacity and mobility induced by the addition of MgO as a promoter. The desorption peaks observed in the O_2-TPD profiles are attributed to the release of weakly bound oxygen species and chemisorbed oxygen that refill surface oxygen vacancies after oxidative pretreatment. The oxygen desorption likely originates from the ZrO_2 and MgO components, both of which are known to form surface oxygen vacancies. The contribution from RhO_x species is considered minimal due to their low content and lack of defined desorption peaks in this temperature range. The O_2-TPD profiles for samples with different MgO loading are presented in Fig. 3. The desorption signals observed below 110 °C are likely associated with physically adsorbed species on the surface [33]. All catalysts exhibited well-defined O_2 desorption peaks in the temperature ranges of 140–235 °C and 345–415 °C. Additionally, the CZrMg15 catalyst exhibited two distinct O_2-TPD signals at 280 °C and 448 °C, whereas the CZr, CMg5, and CZrMg10 catalysts displayed low-intensity O_2 desorption peaks at 495 °C and 650 °C. The peaks observed at 140–235 °C can be attributed to the desorption of molecularly adsorbed O_2, possibly associated with chemically adsorbed O_2 and O_2^- species [32,33], which increases as the

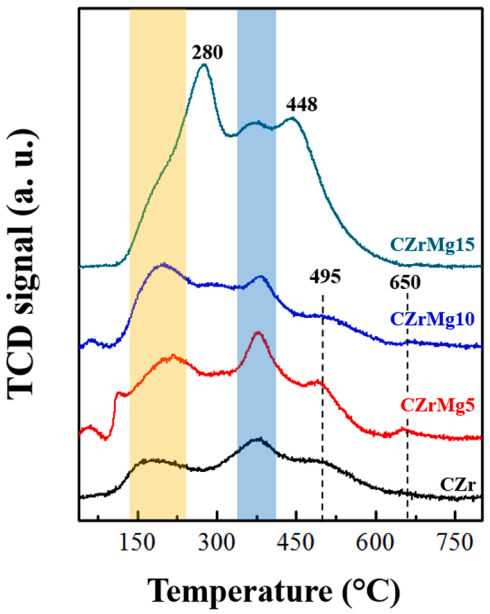

Fig. 3. O_2 -TPD profile for the freshly reduced rhodium catalysts supported on ZrO_2 and on zirconium-magnesium mixed oxides.

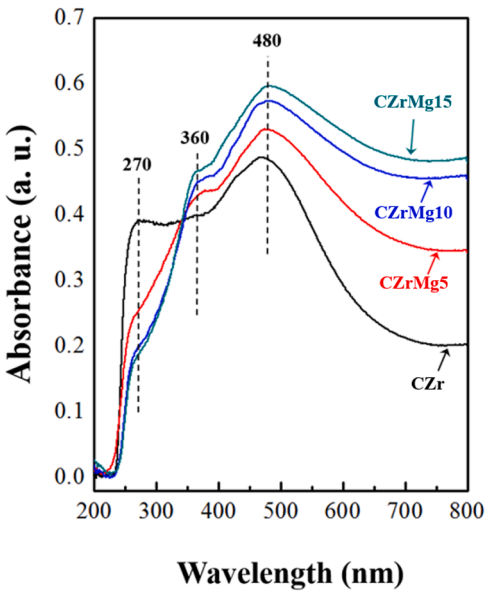

Fig. 4. DRS UV–vis spectra of the reduced rhodium catalysts supported on ZrO_2 and zirconium-magnesium mixed oxides. The electronic spectrum of each catalyst was obtained after subtracting the corresponding support spectrum.

MgO content increases.

The peaks in the range of 345–415 °C are likely due to desorption of chemically adsorbed oxygen from oxygen vacancies or weakly bound surface lattice oxygen [33,34]. Finally, the high-intensity O_2-TPD signal at 280 °C observed in the CZrMg15 catalyst could be associated with desorption of adsorbed oxygen species with stronger interactions [35]. The O_2 desorption peak at 448 °C in this same sample is likely due to oxygen species more strongly adsorbed on oxygen vacancies [35]. Similarly, the low-intensity oxygen desorption signal at 495 °C observed in the CZr, CMg5 and CZrMg10 catalysts may correspond to chemically adsorbed oxygen species with a higher adsorption strength on oxygen vacancies. Finally, the high-temperature signal observed at 650 °C could be associated with lattice oxygen, which requires more energy for removal [33].

The incorporation of MgO significantly enhanced the amount of oxygen adsorbed on the catalyst surface, with the most pronounced increase observed in the catalyst with the highest MgO content. These results indicate that MgO addition not only facilitates the interaction of CO_2 molecules with the surface but also promotes the formation of oxygen vacancies. This effect is further supported by the presence of desorption peaks at higher temperatures, particularly in the catalyst with the highest MgO content.

Fig. 4 presents the DR UV–vis spectra of each reduced catalyst after subtracting the corresponding support spectrum. All samples display two well-defined absorption bands centered at 270 and 480 nm. An additional absorption band around 360 nm was also detected on the MgO-containing catalysts. The high-energy absorption band at 270 nm can be attributed to a ligand-to-metal charge transfer transition ($O^{-2} \rightarrow Zr^{4+}$) [36,37]. This absorption band is strongly influenced by structural defects, such as surface oxygen vacancies [38]. The highest intensity of this band was observed in the MgO-free catalyst (CZr). Upon MgO incorporation, a notable decrease in the intensity of this band was recorded, with a progressive reduction as the MgO content increased, reaching its lowest intensity in the catalyst with an Mg:Zr atomic ratio of 85:15 (CZrMg15). However, the difference in intensity between the CZrMg10 and CZrMg15 catalysts was minimal. The decrease in the intensity of the absorption band at 270 nm may indicate a reduction in the $O^{2-} \rightarrow Zr^{4+}$ charge transfer transition, suggesting a lower concentration of oxygen species susceptible to this transition.

This observation aligns with findings reported by M. Morinaga *et al.* [39], who demonstrated that the $O^{2-} \rightarrow Zr^{4+}$ transition is influenced by the crystallographic structure. Their study reported a decrease in the Zr–O bond distance in the cubic ZrO_2 structure, accompanied by a higher concentration of structural defects compared to other ZrO_2 phases. This reduction in bond length enhances the ionic character of the Zr–O bond, which in turn affects its electronic transitions.

The cubic phase of ZrO_2 is thermally stable at high temperatures (>2300 °C), making its formation challenging at lower temperatures. However, previous studies have successfully synthesized this phase by doping with yttrium [40], which generates a high concentration of oxygen vacancies, leading to the formation of yttrium-stabilized cubic zirconia. Similarly, the addition of MgO facilitates the stabilization of the cubic phase of ZrO_2 by inducing the formation of anion vacancies to maintain charge neutrality, thereby enhancing the electronic stability of the cubic ZrO_2 structure [39,40]. Therefore, it is reasonable to expect an increased number of oxygen vacancies in MgO-doped samples, further contributing to phase stabilization.

Regarding the absorption band at 360 nm, M. Yi et al. [41] reported an absorption feature within the 250–430 nm range, centered around of 360 nm, which was attributed to surface defects in the ZrO_2 structure [39,40]. Therefore, the appearance of the 360 nm band in the MgO-containing samples can be attributed to the formation of oxygen vacancy sites with four electrons (F_2 defect sites) and three electrons (F_2^+ defect centers) [42]. The intensity of this band increased with higher MgO content, indicating that MgO incorporation enhanced the formation of oxygen vacancies.

The band at 480 nm can be attributed to d–d transitions of Rh^{3+} ions in octahedral coordination on the surface or to small Rh oxide particles strongly interacting with the support [43]. The increasing intensity of this band with rising MgO content suggests a higher dispersion or/and a stronger interaction of the Rh species on the surface, likely promoted by MgO incorporation.

H_2-TPR analysis was conducted to assess the influence of MgO on the interaction between rhodium and the catalyst surface. Fig. 5 presents the H_2-TPR profiles of rhodium catalysts supported on ZrO_2 and on ZrO_2−MgO mixed oxides, after reduction up to 600 °C.

The MgO-free catalyst (CZr) exhibits a single reduction peak at 180 °C, attributed to the reduction of Rh^{3+} species weakly interacting with the ZrO_2 surface [44]. This reduction peak shifts to lower temperatures in catalysts with low to moderate MgO content, appearing at 130 °C in

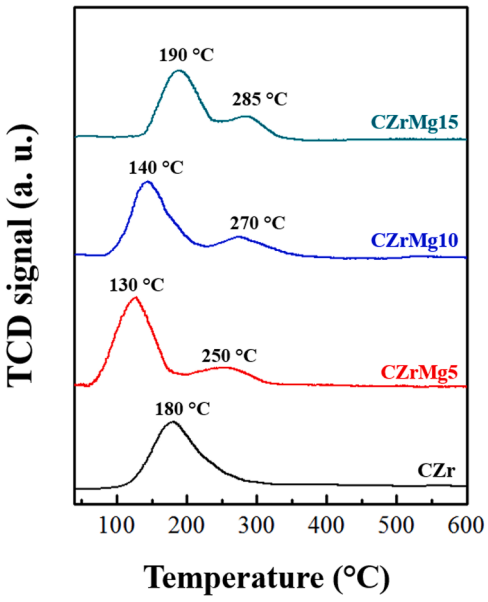

Fig. 5. H_2-TPR profiles of the rhodium catalysts supported on ZrO_2 and zirconium-magnesium mixed oxides.

CZrMg5 and 140 °C in CZrMg10. However, at higher MgO content, this reduction peak shifts to 190 °C, indicating a higher reduction temperature compared to the MgO-free catalyst [44,45]. These results suggest that at low MgO content, the majority of the rhodium species are more easily reducible, even in the catalyst with intermediate MgO content (CZrMg10).

Additionally, catalysts with MgO content also exhibit a secondary reduction peak of lower intensity at higher temperatures, and shifting progressively to higher values (250 °C for CZrMg5, 270 °C for CZrMg10, and 285 °C for CZrMg15). This peak is likely associated with the reduction of Rh species that interact more strongly with the ZrO_2 surface, possibly due to the formation of oxygen vacancies induced by MgO incorporation [44,45]. This is supported by the absorption band observed at 480 nm in the DRS UV–Vis spectra, whose intensity increases with higher MgO content.

These vacancies could possibly contribute to the stabilization of rhodium species on the ZrO_2 surface, making them more resistant to reduction [45,46]. The H_2-TPR profiles therefore indicate that the MgO incorporation enhances the reducibility of Rh species. However, it also promotes the formation of a minor fraction of rhodium species that exhibit stronger interactions with the surface.

To evaluate the size dispersion of rhodium particles and the distribution of different metals in the synthesized catalysts, STEM imaging and chemical mapping were performed. Fig. 6 shows representative TEM images of rhodium catalysts supported on ZrO_2 and ZrO_2−MgO mixed oxides. Additionally, each image includes an inset graph depicting the statistical distribution of particle sizes along with the average particle size. The CZrMg5 and CZrMg10 catalysts exhibits the smallest average particle size, centered at 2.3–2.4 nm, with a narrow distribution, indicating well-dispersed Rh nanoparticles. As the higher MgO content loading, the CZrMg15 catalyst shows an increase in the average particle size, centered at 3.8 nm, with a narrow particle distribution, showing a significant effect of the high MgO loaded on the Rh particle size.

Fig. 7 shows representative STEM images along with elemental mapping by energy-dispersive X-ray spectroscopy (EDS) for the CZrMg5 (a) and CZrMg15 (b) catalysts. The images provide insights into the elemental distribution of Zr, Mg, and Rh on the catalysts surface. Magnesium (red signal) appears well distributed across both catalysts, indicating a uniform dispersion of MgO throughout the surface support. As expected, the density of magnesium oxide species (as indicated by the magnesium mapping intensity) is significantly higher in the CZrMg15 catalyst due to its greater Mg content (Fig. 7b). Rh species (cyan signal) also presents a good dispersion on both CZrMg5 and CZrMg15 catalysts. However, areas with higher rhodium density can also be observed on the surface of the CZrMg15 catalyst (Fig. 7b), suggesting potential agglomeration of Rh particles. This observation aligns with the TEM particle size analysis (Fig. 6c), which showed an increase in Rh particle size with higher MgO concentration.

Fig. 8.

It can be inferred that the MgO incorporation significantly affects the dispersion of Rh species. At low MgO concentrations, the Rh dispersion is enhanced, leading to the formation of smaller particles. In contrast, at higher MgO content (CZrMg15), a higher tendency to aggregation of Rh particles is observed, indicating a shift toward larger particle sizes.

The surface chemical states, as well as the Rh/Zr and Mg/Zr surface atomic ratios of the reduced rhodium catalysts supported on ZrO_2 and Zr–Mg mixed oxides, were investigated by XPS analysis.Fig. 8 shows the Rh 3d core-level spectra obtained by XPS for the reduced catalysts. Table 2 summarizes the binding energies (BE) of the Mg 2p and Rh $3d_{5/2}$ core levels, along with the corresponding surface atomic ratios. The Mg 2p signal, observed at 49.6 ± 0.1 eV, is attributed to Mg^{2+} species in the oxidized state, consistent with the presence of the MgO phase [47,48]. The binding energies of the Rh 3d5/2 core electron levels in the calcined samples are centered on 307.2 eV, characteristic to the presence of metallic Rh^0 species [49].

As shown in Table 2, the surface atomic Mg/Zr ratio increases with the magnesium loading. Specifically, the ratio follows the trend: CZrMg5 (0.013) < CZrMg10 (0.032) < CZrMg15 (0.047), indicating a progressive enrichment of *Mg species* on the catalyst surface as the MgO content increases.

The CZrMg5 catalyst exhibited the highest amount of surface-

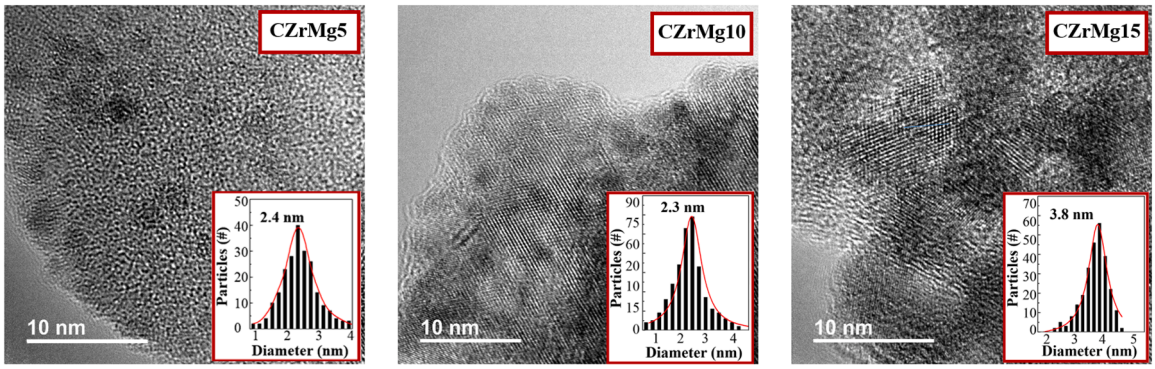

Fig. 6. Representative TEM images of rhodium catalysts supported on ZrO_2 and zirconium-magnesium mixed oxides. Each image includes an inset graph depicting the statistical distribution of particle sizes along with the average particle size.

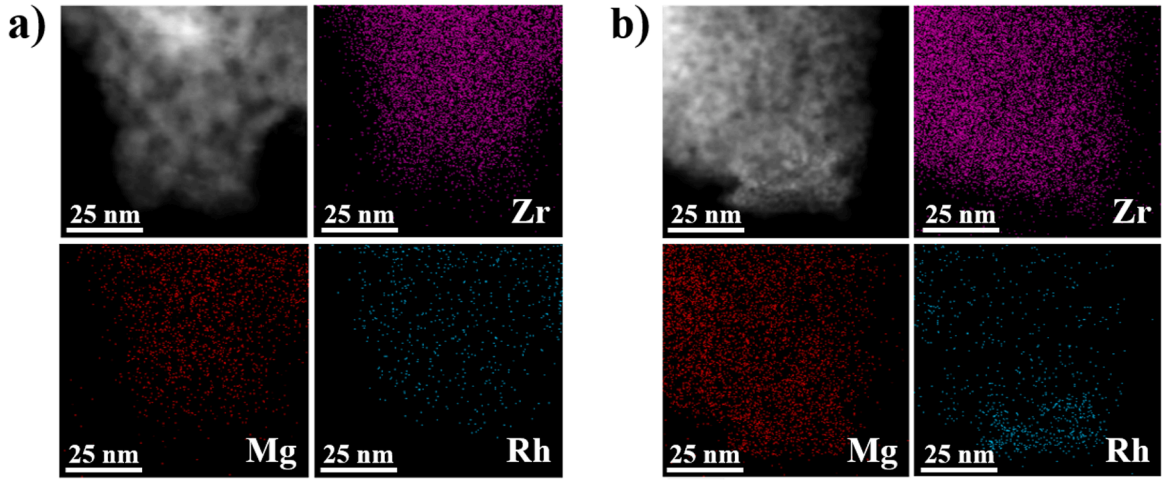

Fig. 7. Representative STEM images and elemental mapping by energy-dispersive X-ray spectroscopy (EDS) for the CZrMg5 (a) and CZrMg15 catalysts (b).

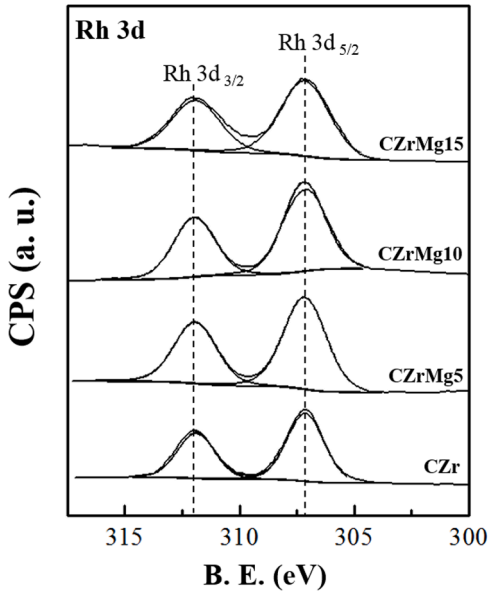

Fig. 8. XPS Rh 3d core level for reduced the rhodium catalysts supported on ZrO_2 and zirconium-magnesium mixed oxides.

Table 2
Binding energies (eV) of core levels and surface atomic ratios for reduced the rhodium catalysts supported on ZrO_2 and zirconium-magnesium mixed oxides.

Sample	Mg 2p	Rh 3d5/2	Surface atomic	
	Mg^{2+}-O	Rh^0	Mg/Zr	Rh/Zr (x10^{-3})
CZr	49.7	307.2	-	6.34
CZrMg5	49.7	71.1	0.013	7.21
CZrMg10	49.6	71.1	0.032	6.73
CZrMg15	49.5	71.2	0.047	5.82

exposed rhodium species among the reduced catalysts, as indicated by the Rh/Zr ratio of 7.21 × 10^{-3}. The Rh/Zr ratio slightly decreases towards higher magnesium contents. It can be concluded that at low magnesium loadings, the surface exposure of rhodium species is enhanced, whereas at higher magnesium contents, a slight decrease in dispersion of Rh species is observed.

3.2. FTIR characterization under reaction conditions

To understand how the incorporation of MgO into Rh/ZrO_2 affects catalytic activity, we analyzed the surface species formed during the catalytic process using FTIR analysis under reaction conditions. Fig. 9 presents the infrared spectra obtained at increasing temperatures under a reactive mixture (3 % CO_2, 12 % H_2, 85 % N_2, vol/vol) passing through the FTIR cell/reactor loaded with the Mg-free ZrO_2-supported Rh catalyst. Upon introducing the reactive mixture at 150 °C, several new bands appeared in the IR spectrum. Specifically, bands at 1575 cm^{-1} and 1388 cm^{-1} were observed, corresponding to the $\nu_{as(COO)}$ and ($\nu s_{(COO+}\delta_{CH)}$ vibration modes of formate species bound to Zr^{4+} sites in a bidentate configuration [50,51].

Additionally, an intense band at 2038 cm^{-1}, along with a shoulder at 1965 cm^{-1}, was detected (Fig. 9). These spectral features correspond to the CO stretching ($\nu_{(CO)}$) vibration modes of CO adsorbed on Rh°, in linear (Rh°–CO) and bridged ((Rh°)$_2$–CO) configurations [4,14]. Both species have been previously reported in CO_2 hydrogenation reactions [4,14]. The formation of formate species likely originates from carbonate intermediates, while the appearance of Rh°-carbonyls may result from CO produced through CO_2 dissociation [14].

Moreover, two weak absorption bands were observed at 3016 cm^{-1} and 1305 cm^{-1}, corresponding to the $\nu_{(-CH)}$ and $\delta_{(-CH)}$ vibration modes of gas-phase methane, respectively [44,45]. The presence of these bands correlates with the temperature range where methane formation was detected in our catalytic tests (shown in the following section). Furthermore, a shoulder at 1620 cm^{-1} appeared in the FTIR spectra, which can be assigned to the $\nu a_{(CO_2)}$ vibration mode of bidentate carbonate species formed on the tetragonal phase of ZrO_2 [44,45].

As the temperature increased, significant changes were observed in the FTIR spectra, as shown in Fig. 9. The bands corresponding to Rh^0-carbonyls (2038 and 1965 cm^{-1}) and formate species (1575 and 1388 cm^{-1}) first slightly intensified, reaching their maximum intensity at 200 °C. Above this temperature, these signals gradually decreased with further heating. Concurrently, the intensity of the bands associated with methane (3016 and 1305 cm^{-1}, Fig. 9) increases markedly in agreement with the levels of catalytic activity expected for the Rh/ZrO_2 sample at this temperature range. The behavior described above could indicate that CO_2 methanation is likely carried out through two distinct pathways: one involving the hydrogenation of Rh-bound carbonyls, and the other involving the hydrogenation of formate species bound to ZrO_2 [14]. The band at 1620 cm^{-1}, attributed to bidentate carbonate species on ZrO_2, exhibits an increase in intensity up to 200 °C while decreasing at higher temperatures [14]. This suggests that these species may be transformed into other surface species, possibly being hydrogenated to

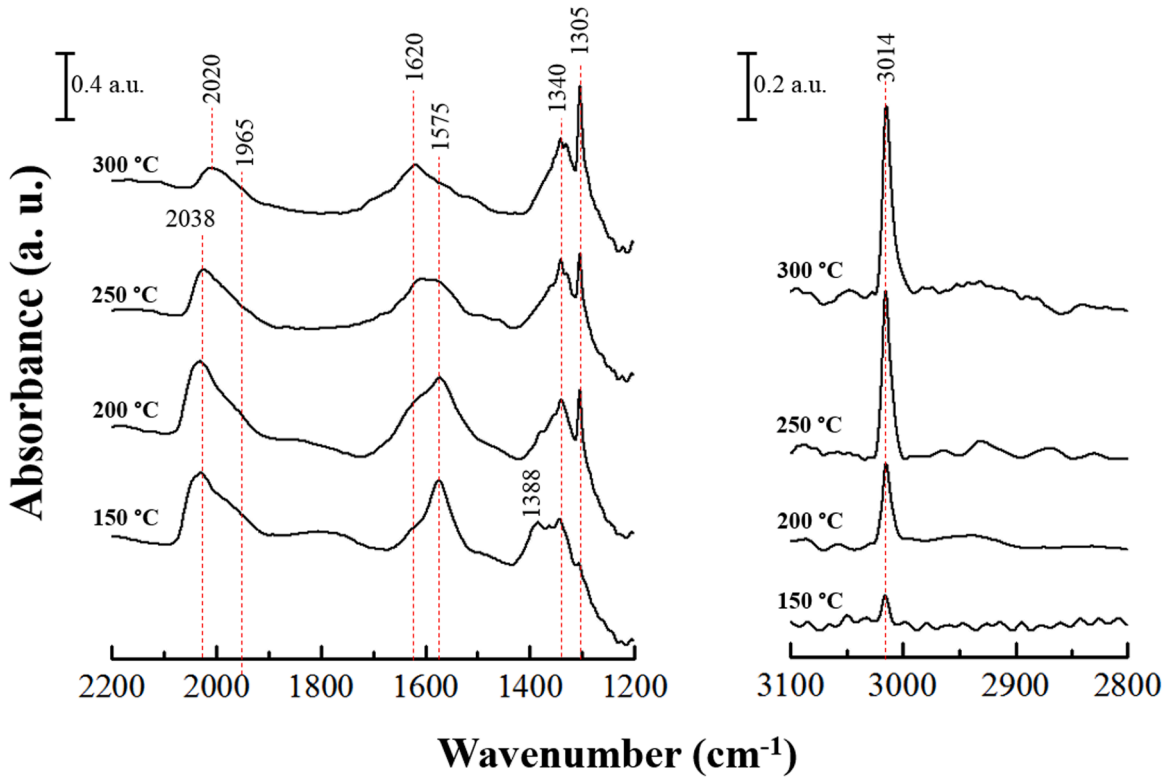

Fig. 9. FTIR characterization of the reduced MgO-free CZr catalyst under reaction conditions (gas mixture of 3 % CO_2/ 12 % H_2/ 85 % N_2 vol/vol) at increasing temperature.

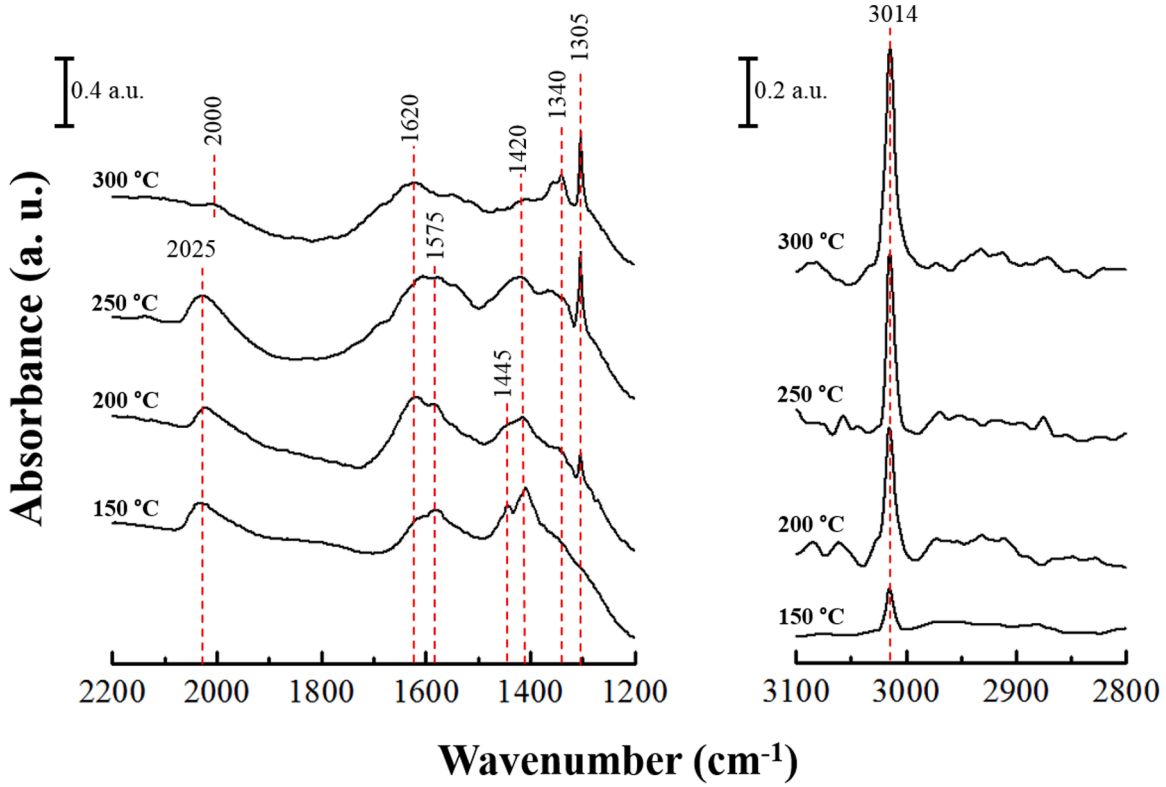

Fig. 10. FTIR characterization of the reduced CZrMg5 catalyst under reaction conditions (gas mixture of 3 % CO_2/ 12 % H_2/ 85 % N_2 vol/vol) at increasing temperature.

formate on the ZrO_2 surface.

During the experiment, a redshift in the Rh^0-CO band from 2038 cm^{-1} to 2020 cm^{-1} was observed when the temperature of reaction was increased to 300 °C. According to previous report [52], this shift can be attributed to a decrease in the CO adsorption coverage on the metallic particles. Additionally, at the beginning of the experiment (150 °C), a band at 1340 cm^{-1} was detected, corresponding to the $\nu a_{(CO_3)}$ vibration of monodentate carbonate species on ZrO_2. This band increased in intensity with rising temperature, suggesting that these species accumulate on the catalyst surface rather than participating in the formation of CH_4.

Fig. 10 presents the FTIR results under reaction conditions for the CZrMg5 catalyst. Notable differences can be observed between the FTIR spectra of CZrMg5 (Fig. 10) and CZr (Fig. 9), despite both catalysts being evaluated under the same reaction conditions. At 150 °C, multiple bands appear in the IR spectrum, indicating the presence of various surface species. The band at 1445 cm^{-1} is assigned to the $\nu s_{(CO_3)}$ vibration of polydentate carbonate species on ZrO_2 [53,54], while the signal at 1420 cm^{-1} corresponds to the $\nu s_{(CO_3)}$ vibration mode of monodentate carbonate species on MgO [55–57]. Additionally, the band at 2025 cm^{-1} is attributed to the stretching vibration of the C–O bond in Rh^0-carbonyls. The presence of formate species on ZrO_2 is confirmed by the bands at 1575 cm^{-1} ($\nu a_{(CO_2)}$) and a shoulder at 1367 cm^{-1} ($\nu s_{(CO_2)}$), which become more pronounced as the temperature increases.

Notably, a signal at 1620 cm^{-1} emerged, which can be assigned to the $\nu a_{(CO_2)}$ vibration of formate species on MgO [58]. This suggests that two distinct types of formate species can form on MgO-containing samples. As previously mentioned, the formation of Rh^0-carbonyls can be attributed to CO adsorption on metallic Rh sites, originating from CO_2 dissociation. In contrast, the formation of formate species is associated with the generation of carbonate intermediates [14].

In the C—H stretching region, a band at 3014 cm^{-1}, assigned to methane ($\nu_{(-CH)}$), was observed (Fig. 10). The presence of this signal aligns with the methane generation temperature observed in the catalytic tests (see next section). As the temperature increases, significant changes were observed in the FTIR spectra of the CZrMg5 catalyst (Fig. 10). Notably, the bands associated with formate species on both ZrO_2 and MgO, as well as those corresponding to Rh^0-carbonyls, intensified, and reaching their maximum intensity between 200 and 250 °C (Fig. 10). This behavior suggests that between 150 and 200 °C, formate species and Rh^0-carbonyls accumulate on the catalyst surface. Above 250 °C, these bands significantly decrease, while the methane band increases in intensity, accompanied by the appearance of a complementary CH_4 band at 1305 cm^{-1} ($\delta_{(-CH)}$). This dynamic evolution indicates that both Rh^0-carbonyls (or desorbed as CO) and formate species (on MgO and ZrO_2) may play a role in methane formation.

The bands associated with carbonate species on ZrO_2 (1445 cm^{-1}, polydentate) and MgO (1420 cm^{-1}, monodentate) increased in intensity up to 250 °C, before diminishing at higher temperatures. This suggests that these species may play a role in the catalytic process, potentially serving as CO_2-adsorbed intermediates that act as precursors to formate species. Additionally, the band at 1340 cm^{-1}, attributed to monodentate carbonate species [52], increased with temperature, suggesting that these species primarily act as spectator species, similar to the case observed on the MgO-free catalyst. Finally, one should note that the intensity of the Rh^0-carbonyl bands in the CZrMg5 catalyst was lower compared to the MgO-free CZr sample (Figs. 9 and 10).

3.2. *Catalyst activity-structure correlation*

The rhodium catalysts supported on ZrO_2 and on ZrO_2−MgO mixed oxides were tested in the CO_2 hydrogenation reaction in a continuous flow-packed bed reactor. Fig. 11 shows the CO_2 conversion and CO selectivity as a function of temperature. In the temperature range studied, all catalysts demonstrated activity in CO_2 hydrogenation, predominantly producing CH_4. As anticipated, increasing the reaction temperature led to higher CO_2 conversion percentages (Fig. 11a).

The MgO-free CZr catalyst exhibited an initial CO_2 conversion of 1.4 % at 175 °C, reaching a maximum of 27.6 % at 325 °C. Introducing a small amount of magnesium notably enhanced CO_2 conversion; the CZrMg5 catalyst achieved the highest conversion across the entire temperature range, reaching 37.8 % of CO_2 conversion at 325 °C. However, higher magnesium contents resulted in decreased CO_2 conversion. The CZrMg15 catalyst showed the lowest conversion, with a maximum of 21.9 % at 325 °C.

All catalysts primarily produced methane. Examining CH_4 selectivity (Fig. 11b) revealed that the magnesium-free CZr catalyst had the lowest CH_4 selectivity, especially at elevated temperatures, reaching 90.1 % at 325 °C. This indicates the formation of a 9.9 % of CO, indicating a more pronounced reverse water-gas shift (RWGS) reaction in this sample at higher temperatures. Incorporating magnesium oxide significantly increased CH_4 selectivity. Notably, the CZrMg15 catalyst, with the highest MgO content, exhibited remarkably high CH_4 selectivity, at just 98.3 % at 325 °C. These findings suggest that incorporating magnesium into the catalyst suppresses the RWGS reaction, favoring methane formation through direct CO_2 hydrogenation. As the MgO content decreased, CH_4 selectivity increased. This trend is attributed not only to lower surface basicity but also to the increased formation of rhodium

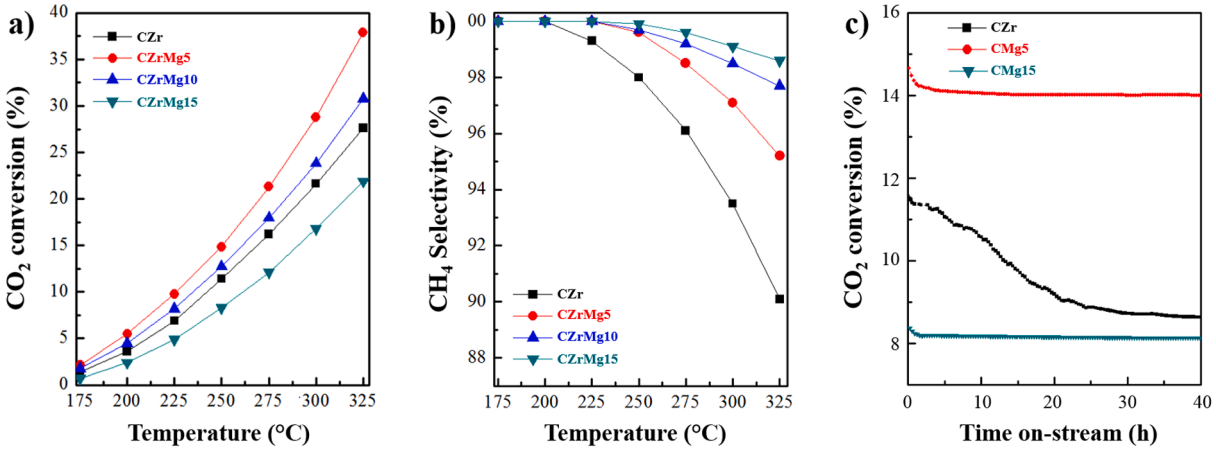

Fig. 11. CO_2 conversion (a) and CH_4 selectivity (b) over rhodium catalysts supported on ZrO_2 and on ZrO_2−MgO mixed oxides. Catalytic stability tests were conducted for the CZr, CZrMg5, and CZrMg15 catalysts under continuous flow conditions at 250 °C for 40 h (c). The catalysts were in situ reduced at 300 °C for 1 hour under a 40 mL/min H_2 flow. The gas hourly space velocity (GHSV) was set at 30,000 h^{-1}, maintaining a 1:4 CO_2:H_2 molar ratio.

carbonyl species in samples with lower MgO loadings. This observation suggests that CO formation is plausibly formed via the reverse water-gas shift (RWGS) reaction, with Rh°–carbonyl species serving as intermediates.

These results indicate that low MgO content enhances catalytic activity in CO_2 conversion. The observed decrease in CO selectivity with increasing MgO content suggests that the MgO incorporation suppresses the RWGS reaction, likely by favoring the associative reaction pathway through formate species over CO_2 dissociation promoting in this way methanation.

To assess the effect of MgO on catalytic stability, long-term tests were conducted for the CZr, CZrMg5, and CZrMg15 catalysts at 250 °C for 48 h (Fig. 11c). The MgO-free catalyst (CZr) exhibited a 25 % loss in activity during the first 20 h of reaction, after which it stabilized, maintaining a CO_2 conversion of 8.7 % for the remainder of the test. In contrast, the MgO-modified catalysts demonstrated significantly improved stability. The CZrMg5 catalyst showed only a 4.1 % activity loss, while the CZrMg15 catalyst, with the highest MgO content, exhibited an even smaller decrease (loss activity of 2.5 %).

As shown in Fig. 10c, all catalysts reached a steady state after approximately 25 h at 250 °C. At this reaction point, CH_4 selectivity was compared with the initial values to evaluate not only conversion stability but also selectivity trends. The CZr catalyst showed a decreases in CH_4 selectivity from 98 % to 95.2 % after 25 h at 250 °C, indicating greater formation of undesirable byproducts (carbon monoxide). In contrast, the MgO-containing catalysts maintained nearly constant CH_4 selectivity, with values of 99.6 % for CZrMg5 and 99.9 % for CZrMg15. These findings indicate that MgO incorporation enhances both catalytic stability and selectivity toward methane, effectively suppressing CO formation. The stabilizing and selective effects of MgO become more pronounced with increasing MgO content in the support.

There is also an increase in the amount of surface oxygen adsorbed on the MgO modified catalysts due to the increase in the amount of surface oxygen vacancies caused by the change in the crystalline structure of the materials favoring the formation of oxygen anions to maintain their neutral charge which in turn facilitates electronic mobility favoring the reduction of adsorbed carbonate species and increasing CO_2 conversion.

The H_2-TPR study showed that in catalysts with low MgO content easily reducible rhodium species compared with the others catalysts, increasing thes CO_2 conversion. However, it was shown that there is a fraction of rhodium species strongly interacting with the surface support as the MgO loaded was increment, affecting its catalytic activity. On the other hand, the particle size distribution indicates that the CZrMg5 and CZrMg10 catalysts possess smaller average particle sizes, as supported by the H_2 consumption observed in the TPR analysis. The higher dispersion of Rh in these samples likely contributes to their enhanced catalytic activity.

The TPD-CO_2 analysis shows that in catalysts with low MgO content there is a strong interaction between the catalyst surface and the CO_2 molecule due to a higher concentration of OH sites and the formation of additional oxygen vacancies, this interaction was losing strength as the amount of MgO added increased due to agglomeration of MgO which in turn is reflected in the catalytic activity where materials with low magnesium content showed better CO_2 conversion. The MgO incorporation increased the basicity properties of the catalysts, particularly weak to moderate ones associated with surface hydroxyl groups and low-coordinated oxygen atoms. The principal CO_2 desorption peak observed in the TPD-CO_2 analysis, initially at lower temperatures for CZr, shifted toward higher temperatures with increasing MgO content, peaking at 130 °C in CZrMg15. This shift indicates stronger CO_2 adsorption, a consequence of enhanced basicity. However, it was also observed that higher MgO coverage in CZrMg15 could cover the zirconia surface and reduce the number of accessible medium-strength basic sites. This behavior correlates with the observed catalytic activity and selectivity. At higher MgO content, CO_2 adsorption increases; however, the stronger interaction of CO_2 with the surface may lead to the formation of more stable, strongly bound CO_2 species. These species may be less reactive, thereby hindering their subsequent conversion to CO and methane.

The catalytic activity observed in CO_2 methanation over Rh-supported catalysts is strongly influenced by the dispersion of Rh species on the support surface. Catalysts with higher Rh dispersion (CZrMg5), exhibit greater surface exposure of active Rh^0 sites, which are essential for efficient H_2 dissociation and subsequent hydrogenation of CO_2-derived intermediates. This is supported by the H_2-TPR profiles and XPS Rh/Zr atomic ratios, which indicate enhanced Rh dispersion at moderate MgO loadings. Consequently, CZrMg5 demonstrated the highest CO_2 conversion (37.8 % at 325 °C), attributable to the higher Rh dispersion and surface basicity. In contrast, at higher MgO contents (CZrMg15), Rh dispersion decreased slightly, leading to reduced catalytic activity. Therefore, the lower amount of MgO incorporation enhances Rh dispersion and catalytic performance.

FTIR analysis under reaction conditions provides comprehensive insights into the performance and selectivity of MgO-enhanced catalysts. The reduction in signal intensity in the area linked to the C—O stretching vibration of Rh° carbonyls in MgO-enhanced catalysts indicates a suppression of the RWGS reaction. This is reflected in a greater preference for methane gas and a lower proportion of CO, depending on the amount of MgO incorporated (CZrMg15 <CZrMg10<CZrMg5<CZr). The bands associated with monodentate and polydentate carbonates in MgO and ZrO_2 emerge alongside the signals linked to formate species. These are regarded as crucial intermediates in the methanation process. This proves the significant function of these carbonates in CO_2 activation, as shown by the enhanced catalytic performance of those catalysts modified with low MgO concentrations (CZrMg5 and CZrMg10).

In this respect, recent DFT studies have clearly emphasized that the formation of oxygen vacancies allows an enhanced charge transfer during CO_2 adsorption compared to pure stoichiometric surfaces leading to significant bending of adsorbed CO_2 [59]. This leads to a higher propensity for CO_2 activation leading in the presence of H_2 to carbonate species which further decompose into *CO adsorbed entities. At this stage, the substoichiometric surface promotes the subsequent hydrogenation into CH_4 while in a final stage, CH_4 desorption allows H_2 to regenerate the oxygen vacancy sites completing the catalytic cycle [60]. These DFT studies therefore are in complete agreement with our present observations.

Notably, the intensity of the Rh°-carbonyl bands in the CZrMg5 catalyst was lower compared to the CZr sample (Figs. 9 and 10). Fig. 12 presents the IR region corresponding to Rh°-CO at 250 °C under reaction conditions, where the highest concentration of carbonyl species was observed on the bare MgO catalyst (CZr). As shown in Fig. 12, a clear trend emerges in which the MgO incorporation leads to a decrease in the intensity of Rh°-CO bands. This indicates that MgO not only alters the crystalline phase of zirconia but also reduces the formation of CO species on Rh° sites, possibly because that magnesium oxide partially inhibits CO_2 dissociation on rhodium sites, preventing their blockage by adsorbed CO (CO_{ads}) and oxygen (O_{ads}) species. This effect could enhance H_2 dissociation on Rh° sites, thereby promoting methane formation through the hydrogenation of formate species.

Furthermore, Fig. 11 shows that the FTIR band corresponding to Rh°–CO species shifts toward lower wavenumbers in catalysts containing MgO, with the lowest frequency observed at 2018 cm^{-1} for the catalyst with the highest MgO content (CZrMg15). This shift is attributed to electronic effects exerted by the support on the Rh particles, indicating stronger Rh–CO interactions as MgO content increases. The enhanced interaction suggests that CO molecules are more tightly bound to Rh sites, potentially leading to site blocking. As a result, the availability of active Rh sites for further CO_2 hydrogenation may be reduced, which could explain the diminished CO formation observed in catalysts with higher MgO loading.

Based on these findings, it is plausible that the reaction proceeds, at

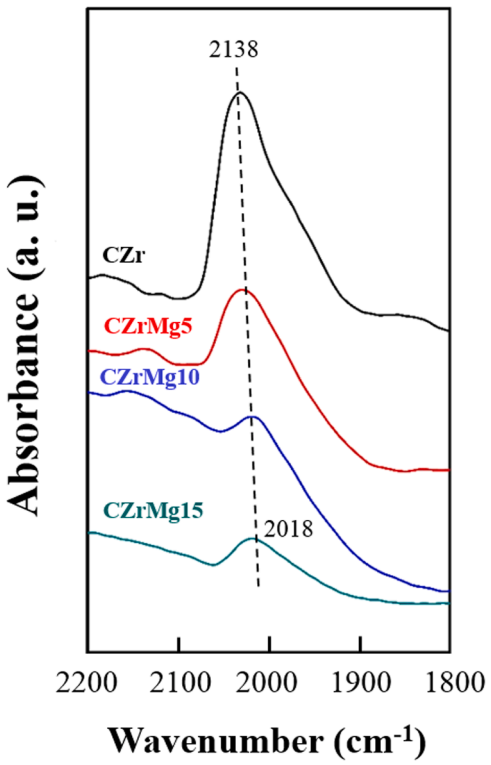

Fig. 12. IR region corresponding to the C–O stretching vibration of Rh⁰ carbonyls, obtained from the FTIR characterization of reduced catalysts under reaction conditions (3 % CO_2, 12 % H_2, 85 % N_2, vol/vol) at 250 °C.

least in part, through a redox mechanism involving surface oxygen vacancies and intermediate transformations such as $CO_2 \rightleftharpoons CO \rightleftharpoons HCOO \rightleftharpoons H$. This hypothesis is supported by the observed oxygen desorption behavior and the known redox properties of zirconia-based supports. The incorporation of MgO notably increases the concentration of oxygen vacancies, which could facilitate such redox processes. These vacancies may not only participate in CO_2 activation but also contribute to the stabilization and transformation of reactive intermediates such as formate and carbonyl species. Operando FTIR analyses provide evidence for the presence of both formate and Rh^0–CO species, which supports the potential involvement of a redox cycle mediated by oxygen and its vacancies, which also aligns with the observed trends in catalytic stability.

4. Conclusions

In this study, MgO-modified ZrO_2 supports were synthesized via the coprecipitation method and subsequently impregnated with 1 wt % Rh to develop catalysts for CO_2 methanation. All catalysts exhibited activity for CO_2 hydrogenation to CH_4 within the temperature range of 175–325 °C under atmospheric pressure in a continuous packed-bed reactor. Notably, the MgO-containing catalysts demonstrated higher selectivity towards CH_4 compared to the unmodified Rh/ZrO_2 reference material. Among them, catalysts with Mg:Zr molar ratios of 5:95 (CZrMg5) and 10:90 (CZrMg10) achieved higher CO_2 conversions.

XRD characterization revealed that MgO incorporation alters the crystallization process of ZrO_2, promoting the formation of the cubic phase in place of the monoclinic structure typically observed in unmodified ZrO_2. This structural modification led to an increase in the surface area and a greater density of weak to moderate basic sites, as confirmed by CO_2-TPD, thereby enhancing CO_2 adsorption. H_2-TPR results further indicated improved Rh reducibility in CZrMg5 and CZrMg10, correlating with their superior catalytic performance.

FTIR characterization under reaction conditions revealed the formation of various surface species during CO_2methanation. For the Rh/ZrO_2 catalyst (CZr), Rh–carbonyls and formate species were identified as key intermediates in CH_4 production. Notably, an increase in MgO content led to a significant decrease in the intensity of Rh–CO bands, suggesting that MgO incorporation suppresses CO formation (formed possibly via RWGS reaction). Instead MgO appears to promote the methanation pathway through the hydrogenation of formate intermediates. These findings indicate that MgO incorporation to ZrO_2 modifies the crystalline structure and the surface chemistry generating an improvement in the catalytic activity of CO_2 methanation.

CRediT authorship contribution statement

F. Ayala-Flores: Writing – original draft, Methodology, Investigation. **R. Huirache-Acuña:** Writing – review & editing, Writing – original draft, Investigation, Formal analysis, Conceptualization. **A. Solís-Garcia:** Writing – original draft, Methodology, Investigation, Formal analysis. **J.C. Fierro-Gonzalez:** Writing – review & editing, Writing – original draft, Investigation, Formal analysis. **Daviel Gómez:** Writing – original draft, Methodology, Investigation, Formal analysis. **Patricia Concepción:** Writing – review & editing, Writing – original draft, Investigation, Formal analysis, Conceptualization. **G. Berhault:** Writing – review & editing, Writing – original draft, Methodology, Investigation, Formal analysis, Conceptualization. **S. Gil:** Methodology, Investigation. **D.Y. López-Chico:** Writing – original draft, Methodology, Investigation, Formal analysis. **E. García-Bordejé:** Writing – original draft, Investigation, Formal analysis. **T.A. Zepeda:** Writing – review & editing, Writing – original draft, Investigation, Formal analysis, Conceptualization.

Declaration of competing interest

The authors declare the following financial interests/personal relationships which may be considered as potential competing interests:

Trino Zepeda reports was provided by National Autonomous University of Mexico. If there are other authors, they declare that they have no known competing financial interests or personal relationships that could have appeared to influence the work reported in this paper.

Acknowledgments

Research funded by PAPIIT-DGAPA, UNAM grant projects IN112922 and IN110125. Thanks to project CONACYT F003 117373 for their partial financial support. R. Huirache-Acuña and G. Berhault want to thank the financial support of SEP-CONACYT-ANUIES-ECOS NORD-322574 and M22P01 Projects. R. Huirache-Acuña acknowledge to CIC UMSNH 2024-2025 and PICIR22-047-C Projects. The authors thank David Dominguez, Erick Flores, Israel Gradilla, Pedro Casillas, and Eloisa Aparicio for technical assistance.

Data availability

Data will be made available on request.

References

[1] D. Yang, F. Xu, D. Jin, X. Meng, A. Lv, W. Dai, R. Zhao, Z. Xin, An efficient Ni-Mg/HNTs catalyst for CO_2 methanation prepared by sol-gel method assisted with citric acid, Mol. Catal. 570 (2025) 114696, https://doi.org/10.1016/j.mcat.2024.114696.

[2] A. Kumar, J. Kaur, M. Ubaidullah, R.K. Gupta, Molecular heterogenous electrocatalysts for CO_2 reduction: science, engineering, challenges and future prospects, Mol. Catal. 561 (2024) 14161, https://doi.org/10.1016/j.mcat.2024.114161.

[3] J. Lin, J. Huang, X. Chen, Y. Zheng, Y. Xiao, Y. Zheng, L. Jiang, Key factors for methane combustion over palladium-based catalysts revealed by enhanced and depressed catalytic performance, Appl. Catal. B Environ. 340 (2024) 123283, https://doi.org/10.1016/j.apcatb.2023.123283.

[4] K.A. Gómez-Flores, A. Solís-García, S.A. Jimenez Lam, M.E. Cervantes-Gaxiola, R. I. Castillo-López, J.P. Ruelas Leyva, S.A. Gómez, E. Flores-Aquino, T.A. Zepeda,

Modulating selectivity in CO_2 methanation through Rhodium catalysts supported on Zirconia-chemically grafted SBA-15, Mol. Catal. 558 (2024), https://doi.org/10.1016/j.mcat.2024.114035.
[5] N. Albeladi, Q.A. Alsulami, K. Narasimharao, Zn deposited nickel silicate nanotubes as efficient CO_2 methanation catalysts, Mol. Catal. 556 (2024) 113949, https://doi.org/10.1016/j.mcat.2024.113949.
[6] R. Ye, X. Wang, Z.-H. Lu, R. Zhang, G. Feng, Construction of robust Ni-based catalysts for low-temperature Sabatier reaction, Chem. Comm. 60 (2024) 11466–11482, https://doi.org/10.1039/d4cc04342a.
[7] Y. Yang, J. Liu, F. Liu, D. Wu, Reaction mechanism of CO_2 methanation over Rh/TiO_2 catalyst, Fuel 276 (2020) 118093, https://doi.org/10.1016/j.fuel.2020.118093.
[8] L. Falbo, M. Martinelli, C.G. Visconti, L. Lietti, C. Bassano, P. Deiana, Kinetics of CO_2 methanation on a Ru-based catalyst at process conditions relevant for power-to-gas applications, Appl. Catal. B: Environ. 225 (2018) 354–363, https://doi.org/10.1016/j.apcatb.2017.11.066.
[9] M. Mihet, M.D. Lazar, Methanation of CO_2 on Ni/γ-Al_2O_3: influence of Pt, Pd or Rh promotion, Catal. Today 306 (2018) 294–299, https://doi.org/10.1016/j.cattod.2016.12.001.
[10] X. Jia, X. Zhang, N. Rui, X. Hu, C.J. Liu, Structural effect of Ni/ZrO_2 catalyst on CO_2 methanation with enhanced activity, Appl. Catal. B: Environ. 244 (2019) 159–169, https://doi.org/10.1016/j.apcatb.2018.11.024.
[11] A. Cárdenas-Arenas, A. Quindimil, A. Davó-Quiñonero, E. Bailón-García, D. Lozano-Castello, U. De-La-Torre, B. Pereda-Ayo, J.A. González-Marco, J. R. González-Velasco, A. Bueno-López, Isotopic and in situ DRIFTS study of the CO_2 methanation mechanism using Ni/CeO_2 and Ni/Al_2O_3 catalysts, Appl. Catal. B: Environ. 265 (2020) 118538, https://doi.org/10.1016/j.apcatb.2019.118538.
[12] R. Zhou, N. Rui, Z. Fan, C.J. Liu, Effect of the structure of Ni/TiO_2 catalyst on CO_2 methanation, Int. J. Hydrogen Energy. 41 (2016) 22017–22025, https://doi.org/10.1016/j.ijhydene.2016.08.093.
[13] Y. Jiang, J. Lang, X. Wu, Y.H. Hu, Electronic structure modulating for supported Rh catalysts toward CO_2 methanation, Catal. Today 356 (2020) 570–578, https://doi.org/10.1016/j.cattod.2020.01.029.
[14] A. Solís-Garcia, T.A. Zepeda, J.C. Fierro-Gonzalez, Spectroscopic evidence of the simultaneous participation of rhodium carbonyls and surface formate species during the CO_2 methanation catalyzed by ZrO_2-supported Rh, Appl. Catal. B: Environ. 304 (2022) 120955, https://doi.org/10.1016/j.apcatb.2021.120955.
[15] M. Zhu, P. Tian, X. Cao, J. Chen, T. Pu, B. Shi, J. Xu, J. Moon, Z. Wu, Y.F. Han, Vacancy engineering of the nickel-based catalysts for enhanced CO_2 methanation, Appl. Catal. B: Environ. 282 (2021) 119561, https://doi.org/10.1016/j.apcatb.2020.119561.
[16] J. Ashok, S. Pati, P. Hongmanorom, Z. Tianxi, C. Junmei, S. Kawi, A review of recent catalyst advances in CO_2 methanation processes, Catal. Today 356 (2020) 471–489, https://doi.org/10.1016/j.cattod.2020.07.023.
[17] X. Guo, D. Gao, H. He, A. Traitangwong, M. Gong, V. Meeyoo, Z. Peng, C. Li, Promotion of CO_2 methanation at low temperature over hydrotalcite-derived catalysts-effect of the tunable metal species and basicity, Int. J. Hydrogen Energy. 46 (2021) 518–530, https://doi.org/10.1016/j.ijhydene.2020.09.19.
[18] X. Guo, Low temperature stability of cubic zirconia, PSS 177 (2000) 191–201, https://doi.org/10.1002/(SICI)1521-396X(200001)177:1<191::AID-PSSA191>3.0.CO;2-X, a.
[19] M.N.C. Lizandra, Mayra P. Alves, Martin Ayala Almeida, D. Caleb, Gary Jacobs Watson, C. Raimundo, Fabio B. Rabelo-Neto, Lisiane V. Noronha, Mattos, CO_2 methanation over metal catalysts supported on ZrO_2: effect of the nature of the metallic phase on catalytic performance, Chem. Eng. Sci. 239 (2021) 116604, https://doi.org/10.1016/j.ces.2021.116604.
[20] T. Iizuka, Y. Tanaka, K. Tanabe, Hydrogenation of CO and CO2 over rhodium catalysts supported on various metal oxides, J. Catal. 76 (1982) 1–8, https://doi.org/10.1016/0021-9517(82)90230-5.
[21] A.P. Bechepeche, O. Treu Jr., E. Longo, C.O. Paiva-Santos, J.A. Varela, Experimental and theoretical aspects of the stabilization of zirconia, J. Mater. Sci. 34 (1999) 2751–2756, https://doi.org/10.1023/A:1004698026465.
[22] M. Yan, Y. Li, G. Yin, S. Tong, J. Chen, Synthesis and characterization of a MgO-$MgAl_2O_4$-ZrO_2 composite with a continuous network microstructure, Ceram. Int. 43 (2017) 5914–5919, https://doi.org/10.1016/j.ceramint.2017.01.082.
[23] L. Kong, S. Zhu, Q. Bi, Z. Qiao, J. Yang, W. Liu, Friction and wear behavior of self-lubricating ZrO_2 (Y_2O_3)–CaF_2–Mo–graphite composite from 20°C to 1000°C, Ceram. Int. 40 (2014) 10787–10792, https://doi.org/10.1016/j.ceramint.2014.03.068.
[24] K. Li, J. Chen, J. Peng, S. Koppala, M. Omran, G. Chen, One-step preparation of CaO-doped partially stabilized zirconia from fused zirconia, Ceram. Int. 46 (2020) 6484–6490, https://doi.org/10.1016/j.ceramint.2019.11.129.
[25] Y.J. Xia, J.L. Song, D.N. Yuan, X.N. Guo, X. Guo, Synthesis and characterization of one-dimensional metal oxides: TiO_2, CeO_2, Y_2O_3-stabilized ZrO_2 and $SrTiO_3$, Ceram. Int. 41 (2015) 533–545, https://doi.org/10.1016/j.ceramint.2014.08.102.
[26] A. Rizzetto, E. Sartoretti, M. Piumetti, R. Pirone, S. Bensaid, Novel application of Ru-based catalysts on MgAl oxides alkaline adsorbents for cyclic CO_2 methanation, Chem. Eng. J. 501 (2024) 157585, https://doi.org/10.1016/j.cej.2024.157585.
[27] M.C. Bacariza, I. Graça, S.S. Bebiano, J.M. Lopes, C. Henriques, Magnesium as promoter of CO_2 methanation on Ni-based USY zeolites, Energy Fuels 31 (2017) 9776–9789, https://doi.org/10.1021/acs.energyfuels.7b01553.
[28] N.C. Horti, M.D. Kamatagi, S.K. Nataraj, M.N. Wari, S.R. Inamdar, Structural and optical properties of zirconium oxide (ZrO_2) nanoparticles: effect of calcination temperature, Nano Express 1 (2020) 010022, https://doi.org/10.1088/2632-959x/ab8684.
[29] X. Guo, Low temperature stability of cubic zirconia, PSS 177 (a) (2000) 191–201, https://doi.org/10.1002/(SICI)1521-396X(200001)177:1<191::AID-PSSA191>3.0.CO;2-X.
[30] M. Yan, Y. Li, G. Yin, S. Tong, J. Chen, Synthesis and characterization of a MgO-$MgAl_2O_4$-ZrO_2 composite with a continuous network microstructure, Ceram. Int. 43 (2017) 5914–5919, https://doi.org/10.1016/j.ceramint.2017.01.082.
[31] J. Qiu, B. Zhou, Q. Yang, Y. Liu, L. Zhang, B. Wang, S. Song, J. Zhang, S. Huang, J. Chen, L. Lin, X. Zeng, Efficient catalytic transfer hydrogenation of furfural and other biomass-derived compounds over sustainable magnetic catalyst, Fuel Process. Technol. 254 (2024) 108010, https://doi.org/10.1016/j.fuproc.2023.108010.
[32] P. Li, C. He, J. Cheng, C.Yan Ma, B. Juan Dou, Z.Ping Hao, Catalytic oxidation of toluene over Pd/Co_3AlO catalysts derived from hydrotalcite-like compounds: effects of preparation methods, Appl. Catal. B: Environ. 101 (2011) 570–579, https://doi.org/10.1016/j.apcatb.2010.10.030.
[33] Q. Huang, Y. Lu, H. Si, B. Yang, T. Tao, Y. Zhao, M. Chen, Study of complete oxidation of formaldehyde over MnO_x–CeO_2 mixed oxide catalysts at ambient temperature, Catal Lett 148 (2018) 2880–2890, https://doi.org/10.1007/s10562-018-2479-0.
[34] H. Huang, Y. Gu, J. Zhao, X. Wang, Catalytic combustion of chlorobenzene over VO_x/CeO_2 catalysts, J. Catal. 326 (2015) 54–68, https://doi.org/10.1016/j.jcat.2015.02.016.
[35] H. Liang, Y. Hong, C. Zhu, S. Li, Y. Chen, Z. Liu, D. Ye, Influence of partial Mn-substitution on surface oxygen species of $LaCoO_3$ catalysts, Catal. Today 201 (2013) 98–102, https://doi.org/10.1016/j.cattod.2012.04.036.
[36] X. Xu, Y. Tong, J. Huang, J. Zhu, X. Fang, J. Xu, X. Wang, Insights into CO_2 methanation mechanism on cubic ZrO2 supported Ni catalyst via a combination of experiments and DFT calculations, Fuel 283 (2021) 118867, https://doi.org/10.1016/j.fuel.2020.118867.
[37] F. Davar, N. Shayan, A. Hojjati-Najafabadi, V. Sabaghi, S. Hasani, Development of ZrO_2-MgO nanocomposite powders by the modified sol-gel method, Int. J. Appl. Ceram. Technol. 14 (2016) 211–219, https://doi.org/10.1111/ijac.12624.
[38] Y.-F. Lin, F.-L. Liang, ZrO_2/carbon aerogel composites: a study on the effect of the crystal ZrO_2 structure on cationic dye adsorption, J. Taiwan Inst. Chem. Eng. 65 (2016) 78–82, https://doi.org/10.1016/j.jtice.2016.05.015.
[39] M. Morinaga, H. Adachi, M. Tsukada, Electronic structure and phase stability of ZrO_2, J. Phys. Chem. Solids 44 (1983) 301–306, https://doi.org/10.1016/0022-3697(83)90098-7.
[40] J. Faber Jr., M.H. Mueller, B.R. Cooper, Neutron-diffraction study of Zr(Ca,Y)$O_{(2-x)}$ evidence of differing mechanisms for internal and external distortions, Phys. Rev. B 17 (1978) 4884–4888, https://doi.org/10.1103/PhysRevB.17.4884.
[41] M. Yi, Y. Zhang, J. Xu, D. Deng, Z. Mao, X. Meng, X. Shi, B. Zhao, Surface-enhanced Raman scattering activity of ZrO_2 nanoparticles: effect of tetragonal and monoclinic phases, Nanomaterials 11 (2021) 2162, https://doi.org/10.3390/nano11092162.
[42] X. Li, J. Zhao, X. Hong, Y. Yang, X. Tang, Y. Zhu, T. Li, Calcination-dependent surface defect variation and antibacterial activity of magnesium oxide nanoplates, Chemistry Select 5 (2020) 3201–3207, https://doi.org/10.1002/slct.201904853.
[43] J. Kuncewicz, B. Ohtani, Rhodium-doped titania photocatalysts with two-step bandgap excitation by visible light—Influence of the dopant concentration on photosensitization efficiency, RSC Adv 6 (2016) 77201–77211, https://doi.org/10.1039/C6RA09364G.
[44] J. Chen, L. Qiao, Z. Zhou, X. Wu, X. Guo, S. Zong, Y. Ding, Y. He, Y. Yao, Promoted hydroformylation of formaldehyde by electronic metal–Support interactions in N-group functionalized silica supported rhodium catalyst, Catal. Letters 151 (2021) 36664, https://doi.org/10.1007/s10562-021-03568-x. -3674.
[45] A. Cervantes Uribe, G.A. Del Angel Montes, G. Torres-Torres, A. Vázquez-Zavala, F. González-García, A. Cordero-García, R. Ojeda-López, Correlation of Rh particle size with CO chemisorption: effect on the catalytic oxidation of MTBE, J. Compos. Sci. 3 (2019) 81, https://doi.org/10.3390/jcs3030081.
[46] Wei-Zheng Weng, Xiao-Qing Pei, Jian-Mei Li, Chun-Rong Luo, Ying Liu, Hai-Qiang Lin, Chuan-Jing Huang, Hui-Lin Wan, Effects of calcination temperatures on the catalytic performance of Rh/Al_2O_3 for methane partial oxidation to synthesis gas, Catal. Today 117 (2006) 53–61, https://doi.org/10.1016/j.cattod.2006.05.011.
[47] H.-H. Huang, W.-C. Shih, C.-H. Lai, Nonpolar resistive switching in the Pt/MgO/Pt nonvolatile memory device, Appl. Phys. Lett. 96 (2010) 193505, https://doi.org/10.1063/1.3429024.
[48] J.S. Valente, E. Lima, J.A. Toledo-Antonio, M.A. Cortes-Jacome, L. Lartundo-Rojas, R. Montiel, J. Prince, Comprehending the thermal decomposition and reconstruction process of sol-gel MgAl layered double hydroxides, *J. Phys. Chem. C* 114 (2010) 2089–2099, https://doi.org/10.1021/jp910538r.
[49] K. Zheng, B. Liu, Y. Xu, X. Liu, Effect of Rh loading on the selectivity to methanol and ethanol in the hydrogenation of CO_2 over the Rh/CeO_2 catalyst, J. Fuel. Chem. Tech. 52 (2024) 1214–1223, https://doi.org/10.1016/S1872-5813(24)60450-0.
[50] E.M. Mendoza-Núñez, J.C. Fierro-Gonzalez, T.A. Zepeda, A. Solis-Garcia, Effect of platinum addition on the reaction mechanism of the CO_2 methanation catalyzed by ZrO_2-supported Rh, Molecular Catalysis 533 (2022) 112801, https://doi.org/10.1016/j.mcat.2022.112801.
[51] Z.-Y. Ma, C. Yang, W. Wei, W.-H. Li, Y.-H. Sun, Surface properties and CO adsorption on zirconia polymorphs, J. Mol. Catal. A Chem. 227 (2005) 119–124, https://doi.org/10.1016/j.molcata.2004.10.017.
[52] A. Solís-Garcia, J.F. Louvier-Hernandez, A. Almendarez-Camarillo, J.C. Fierro-Gonzalez, Participation of surface bicarbonate, formate and methoxy species in the carbon dioxide methanation catalyzed by ZrO_2-supported Ni, Appl. Catal. B: Environ. 218 (2017) 611–620, https://doi.org/10.1016/j.apcatb.2017.06.063.

[53] H.-Y.Tiffany Chen, S. Tosoni, G. Pacchioni, A DFT study of the acid–base properties of anatase TiO_2 and tetragonal ZrO_2 by adsorption of CO and CO_2 probe molecules, Surf. Sci. 652 (2016) 163–171, https://doi.org/10.1016/j.susc.2016.02.008.
[54] K. PokrovskiKyeong Taek J.T. Bell, Investigation of CO and CO_2 adsorption on tetragonal and monoclinic zirconia, Langmuir 17 (2001) 4297–4303, https://doi.org/10.1021/la001723z.
[55] H. Bekhti, Y. Boucheffa, A.H. Ait Blal, A. Travert, In situ FTIR investigation of CO_2 adsorption over MgO–Impregnated NaY zeolites, Vib. Spectrosc. 117 (2021) 103313, https://doi.org/10.1016/j.vibspec.2021.103313.
[56] R. Philipp, K. Fujimoto, FTIR spectroscopic study of carbon dioxide adsorption/desorption on magnesia/calcium oxide catalysts, J. Phys. Chem. 96 (1992) 9035–9038, https://doi.org/10.1021/j100201a063.
[57] D. Cornu, H. Guesmi, J.-M. Krafft, H. Lauron-Pernot, Lewis Acido-basic interactions between CO2 and MgO surface: DFT and DRIFT approaches, J. Phys. Chem. C 116 (2012) 6645–6654, https://doi.org/10.1021/jp211171t.
[58] H. Borchert, B. Jürgens, V. Zielasek, G. Rupprechter, S. Giorgio, C.R. Henry, M. Bäumer, Pd nanoparticles with highly defined structure on MgO as model catalysts: an FTIR study of the interaction with CO, O_2, and H2 under ambient conditions, J. Catal. 247 (2007) 145–154, https://doi.org/10.1016/j.jcat.2007.02.002.
[59] P. Pratap Singh, A.P Shweta Kamaliny, K. Ray, S. Sengupta, The pivotal role of oxygen vacancy and surface hydroxyl in the adsorption and activation of CO_2 on ceria-zirconia mixed oxide, Molecular Catal. 555 (2024) 113855, https://doi.org/10.1016/j.mcat.2024.113855.
[60] H. Li, Y. Tang, W. Yan, M. Liu, Z. Wang, J. Li, Feng Yu, Vacancy-enhanced photothermal activation for CO2 methanation on Ni/SrTiO3 catalysts, Appl. Catal. B: Environ. Ener. 357 (2024), https://doi.org/10.1016/j.apcatb.2024.124346.